

Research Article

Comparative Study of Indentation Size Effects in As-Sintered Alumina and Alumina Shock Deformed at 6.5 and 12 GPa

Riya Chakraborty,¹ Anoop K. Mukhopadhyay,¹ Keshaw D. Joshi,² Amit Rav,²
Ashok K. Mandal,¹ Sandip Bysakh,¹ Sampad K. Biswas,¹ and Satish C. Gupta²

¹ CSIR-Central Glass and Ceramic Research Institute, 196, Raja S.C. Mullick Road, Kolkata 700032, India

² Applied Physics Division, Bhabha Atomic Research Centre, Mumbai 400085, India

Correspondence should be addressed to Anoop K. Mukhopadhyay, anoopmukherjee@cgcri.res.in

Received 10 September 2012; Accepted 30 September 2012

Academic Editors: S.-S. Lin and P. Thavorniti

Copyright © 2012 Riya Chakraborty et al. This is an open access article distributed under the Creative Commons Attribution License, which permits unrestricted use, distribution, and reproduction in any medium, provided the original work is properly cited.

Nanohardness of alumina ceramics determines its performance in all contact-related applications because the issue of structural integrity gets determined at the nanoscale of contact. In spite of the wealth of the literature, however, it is not yet known in significant details how the high-strain rate flyer-plate impact at different pressure affects the nanohardness of dense, coarse grain alumina ceramics. Thus, the load controlled nanoindentation experiments were performed with a Berkovich indenter on an as-received coarse grain ($\sim 10\ \mu\text{m}$), high density ($\sim 3.98\ \text{gm}\cdot\text{cc}^{-1}$) alumina, and shock recovered tiny fragments of the same alumina obtained from gas gun experiments conducted at 6.5 GPa and 12 GPa shock pressures with stainless steel flyer plates. The nanohardness of the as-received alumina was much higher than that of the 6.5 GPa and 12 GPa shock-recovered alumina. The indentation size effect (ISE) was the strongest in alumina shocked at 12 GPa and strong in alumina shocked at 6.5 GPa, but it was mild in the as-received alumina sample. These results were rationalized by analysis of the experimental load depth data and evidences obtained from field emission scanning electron microscopy. In addition, a rational picture of the nanoindentation responses of the as-received and shocked alumina ceramics was provided by a qualitative model.

1. Introduction

The combination of high hardness and high compressive strength makes alumina ceramics a good candidate for a very high strain rate damage resistant applications [1–27]. Consequently, the shock deformation behaviour and characterization of shock recovered alumina ceramics has emerged as a major area of active research [1–4]. As hardness determines the contact damage resistance, it is extensively studied at macro- or microscale [5–7] as well as at the nanoscale [8, 9], although most of these measurements [6–9], barring a few [5], are on fine grain and/or submicrometer grain-sized alumina ceramics. The hardness of alumina [10–12] shows the indentation size effect (ISE), whereby a unique hardness data of alumina for design purpose become difficult to obtain. The proposed explanations [14–25] have not yet been completely successful to unequivocally establish the genesis of ISE in structural ceramics [13, 26].

Recently, an explanation for the observation of strong ISE in nanohardness of alumina shocked at 6.5 GPa was reported by us [28]. The objective of the present work is to examine the presence of ISE in nanohardness of alumina shocked at 12 GPa and compare the results with those of alumina shocked at 6.5 GPa [28] so that a generic mechanism of ISE in nanohardness of shock-loaded alumina can be provided.

2. Materials and Methods

The experimental details have been already reported in [27–31] and will be only briefly mentioned here. The sintered alumina discs (diameter $\sim 50\ \text{mm}$, thickness $\sim 2.48\ \text{mm}$) of $10\ \mu\text{m}$ grain size and 99.95% theoretical density had a Hugoniot elastic limit (HEL) of 1.91 GPa [27]. The shock recovery experiments were conducted by an asymmetric flyer plate impact with a SS304 plate at 6.5 and 12 GPa shock pressures in a 63 mm bore two-stage gas gun [27–31]. The

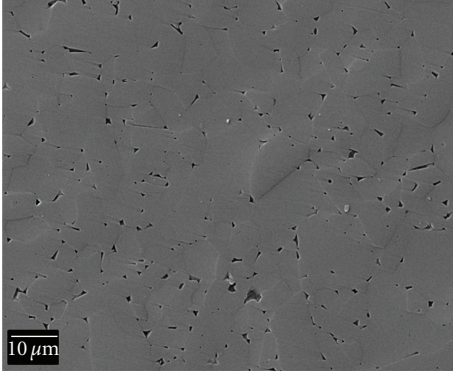


FIGURE 1: Microstructure of the 10 μm alumina ceramic.

nanohardness (H) and Young's moduli (E) of as-received alumina (ARA) and shocked alumina (SA) samples were evaluated following the well-established Oliver-Pharr [32] method from the load (P) versus depth (h) plots obtained during the load controlled nanoindentation experiments at 10–1000 mN in a commercial machine (Fischerscope H100-XYp; Fischer, Switzerland) that was equipped with a Berkovich nanoindenter of tip radius ~ 150 nm and semiapex angle $\sim 65.3^\circ$ and had resolutions of $\pm 0.2 \mu\text{N}$ and ± 1 nm for load and depth measurements, respectively. A 5×5 matrix array of nanoindents was made at five different, randomly chosen locations in the alumina surface. The damage initiation and their evolution around the nanoindents at the submicrostructural length scale of ARA and SA samples were studied using a field emission scanning electron microscope, FE-SEM (Supra VP35 Carl Zeiss, Germany).

3. Results and Discussions

The general microstructure of the 10 μm alumina sample is shown in Figure 1. At a typical load of 500 mN the P - h plots for ARA, 6.5 GPa, and 12 SA samples (Figure 2(a)) exhibited the characteristic elastoplastic behavior typical of structural ceramics. The nanohardness of ARA had a very slight fall with increase in depth (Figure 2(b)), whereas that of 6.5 GPa SA had a sharper fall and that of 12 GPa SA had the sharpest fall with depth (Figure 2(a)). The decrease in nanohardness with depth is termed as the indentation size effect (ISE). Thus, the ISE was very mild in ARA but quite strong in 6.5 GPa SA and the strongest in 12 GPa SA sample. As a result, the nanohardness of 6.5 GPa SA was decreased by as much as 25% but that of the 12 GPa SA was decreased by as much as 33% with respect to that of the ARA samples. Therefore, depending on the presence or absence of shock induced microstructural defects, the alumina ceramics may reveal both mild and strong ISE. Among the models [10–25] which attempt to explain ISE, the most well-established model is the Nix and Gao [15] model. Depending on the strain gradient plasticity concept, this model, [15] tried to explain ISE on the premise that the deformation process is

controlled basically by formation, storage, and movement of dislocations. According to [15]:

$$H^2 = H_0^2 \left(1 + \frac{h^*}{h} \right), \quad (1)$$

where H is the experimentally measured nanohardness at a depth h , and h^* is a “characteristic length” up to which the maximum rate of change in nanohardness with depth would happen, and H_0 is the hardness at infinite depth [15]. The fitting of the present experimental data to (1) yielded for the ARA sample $H_0 = 19.93$ GPa and $h^* = 9$ nm. In this case, the ratio of h/G (where G denotes the grain size) was 0.0009, which is negligibly small. However, for the 6.5 GPa SA sample, H_0 was 13.40 GPa, and h^* was 165.6 nm, but in the case of 12 GPa SA sample, H_0 was 11.12 GPa, and h^* was 118.2 nm. Thus, for 6.5 GPa and 12 GPa SA samples, the ratio of h/G had jumped to as high as 0.02 and 0.01, respectively. These h/G values were two orders of magnitude higher than that of the ARA sample. Although there were differences in material preparation and measurement techniques with respect to those of the present work, the predicted value of H_0 and h^* obtained from the present experimental data of ARA samples matched well with the reported hardness values of alumina [5–7, 13, 33]. However, the characteristic length scales of h^* , that is, 165.6 nm and 118.2 nm, for the cases of 6.5 GPa and 12 GPa SA samples were both a little higher than the prescribed depth of 100 nm [34] up to which the gradient in local strain would affect the nanohardness data the maximum.

The loading cycle of the present nanoindentation depth (h) and the applied load (P) can be expressed by the following empirical equation [35]:

$$P = Ch^n, \quad (2)$$

where, C and n are constants. These constants can be determined from fitting of the experimental data to (2). Such an approach was proposed [35] to explain the presence of ISE in single crystal 8Y-FSZ and polycrystalline 12Ce-TZP ceramics. It was proposed further [35] that if $n = 2$ in (2), the materials would show no ISE. A similar view was also expressed by other researchers [36, 37]. On the other hand, it is expected that if $n < 2$ then the material would obviously show ISE [35–37]. Further, by taking the second-order differentiation of P with respect to h of (2), we obtain the following equation [35]:

$$\frac{d^2P}{dh^2} = n(n-1) \cdot C \cdot h^{n-2}. \quad (3)$$

From (3), it is clear that d^2P/dh^2 will be a constant, when $n = 2$. This situation will occur when there is no ISE. However, when $n < 2$, there will be a decrease of d^2P/dh^2 with increase of h thereby confirming the presence of ISE. Figures 3(a)–3(c) represent the fitting of (2) to the loading cycles of the present experimental P - h data for the ARA, 6.5 GPa SA, and 12 GPa SA samples at three different typical, illustrative loads of 500, 700, and 1000 mN. The goodness of fit was better than 0.99 for all the three samples. This

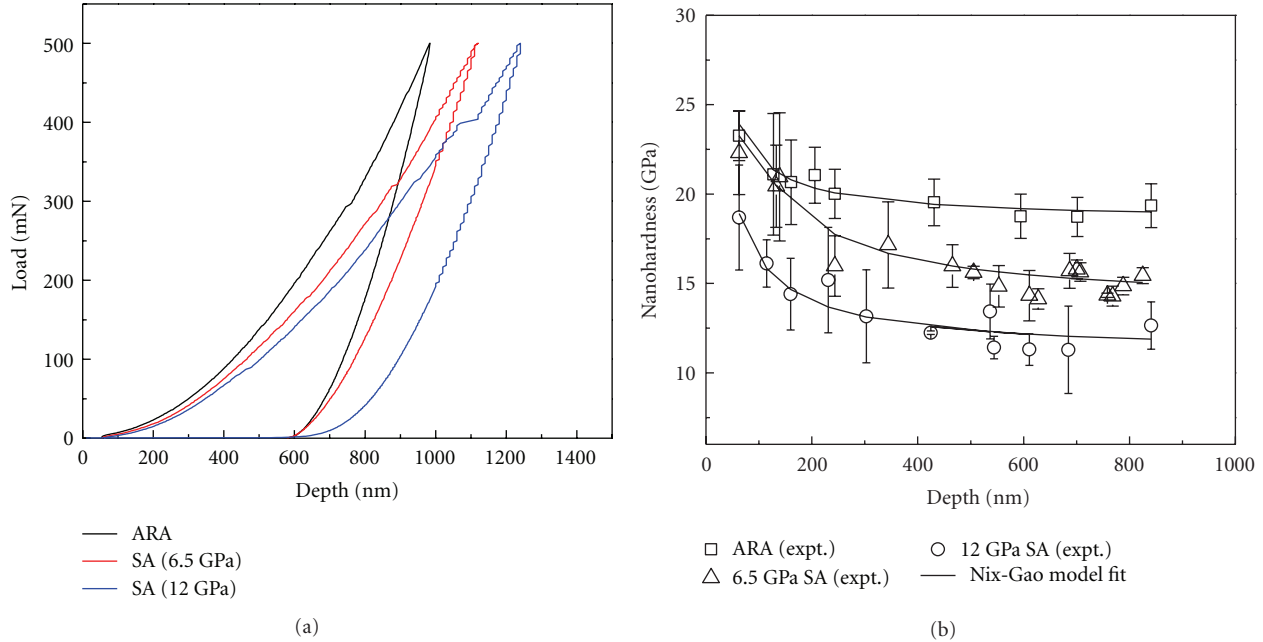


FIGURE 2: (a) Load-depth plots at a typical illustrative load of 500 mN and (b) nanohardness (H) versus depth (h) plots for ARA, 6.5 GPa SA, and 12 GPa SA samples. The solid lines depict the predicted variation according to the Nix and Gao Model [15].

evidence confirmed that the empirical equation (2) gives a good description of the loading cycle of P - h plots for ARA, 6.5 GPa SA, and 12 GPa SA samples. It was also observed (Figure 3) that at a given load, the depths of penetrations of both of the SA samples were higher than that of the ARA samples. This fact implied that the SA samples had more inherent weakness as compared to those of the ARA sample. Further, the power law exponent (n) values were very slightly lesser than 2 in case of ARA samples at different loads, whereas for SA samples, it was observed that the n values became $\ll 2$ as the shock pressure increases. This data provide a first-order clue as to why there was the presence of a strong ISE in the SA samples used in the present work.

In Figure 4, (3) is fitted to the experimental P - h data obtained during loading cycles of the nanoindentation experiments on ARA, 6.5 GPa SA, and 12 GPa SA samples at typical, illustrative loads of 500 and 1000 mN. The relative percentages of changes in second-order derivative of (2), for example, d^2P/dh^2 versus depth (h) at different portions of the plots along AB, BC, and CD regions in Figures 4(a) and 4(b), are shown in Table 1 for both ARA as well as 6.5 GPa and 12 GPa SA samples. Further, from Figures 4(a) and 4(b), it is also seen that d^2P/dh^2 decreased continuously with depth for ARA, and both the SA samples as $n < 2$. In addition, it may be observed from Table 1 and Figures 4(a) and 4(b) that at comparable intervals of the depths of penetration for example, at regions AB, BC, and CD, the relative percentages of changes in d^2P/dh^2 with respect to the depth h were much higher for both the SA samples as compared to those of the ARA samples. This data again strongly suggested that the SA samples were more compliant in nature than the ARA sample, and the 12 GPa SA sample showed much more compliance than the 6.5 GPa SA sample.

There was the presence of relatively much larger number of serrations, that is, nanoscale displacement jumps, which signify the occurrence of “multiple micro-pop-in” in the load-depth plots of 12 GPa SA sample during the loading cycle in comparison to those of the 6.5 GPa SA sample, Figures 5(a)–5(d). In contrast, there were negligible serrations observed in ARA sample compared to the presence of those in both of the SA samples, Figures 5(a), 5(b), 5(c), and 5(d). The reason of such observation was shown by the present author and coworkers [28] to be linked to (a) the initiation of nanoscale plasticity events and (b) the more intense interaction between the penetrating nanoindenter and the preexistent as well as shock-induced microstructural damages that lead to highly localized microcrack formation in the vicinity of the nanoindent in the SA samples. The present results (Figures 2–5) confirmed that this interaction was much more intense in the case of the 12 GPa SA sample than in the case of the 6.5 GPa SA sample. Similar observations were also reported for a large variety of materials such as quartz, soda-lime glass, fused silica, and glassy carbon [38–41] as well as sapphire [42], GaN [43], and ZnO [44]. In the case of sapphire, the genesis of the pop-in events was ascribed to activation of rhombohedral twinning under a penetrating nanoindenter. The theoretical modeling work by other researchers [25] has suggested that ISE would be more pronounced when slip bands are oriented parallel to the surface as compared to the case when there is nonparallel slip band orientation. Further supportive evidence to such picture indeed emerges from the FE-SEM photomicrographs of the nanoindents in the SA sample which showed relatively predominant presence of slip lines, deformation bands, and microcracks (Figures 6(b) and 6(c)), while on a comparative scale, such features were absent in the as received alumina (Figure 6(a)). Therefore, based on

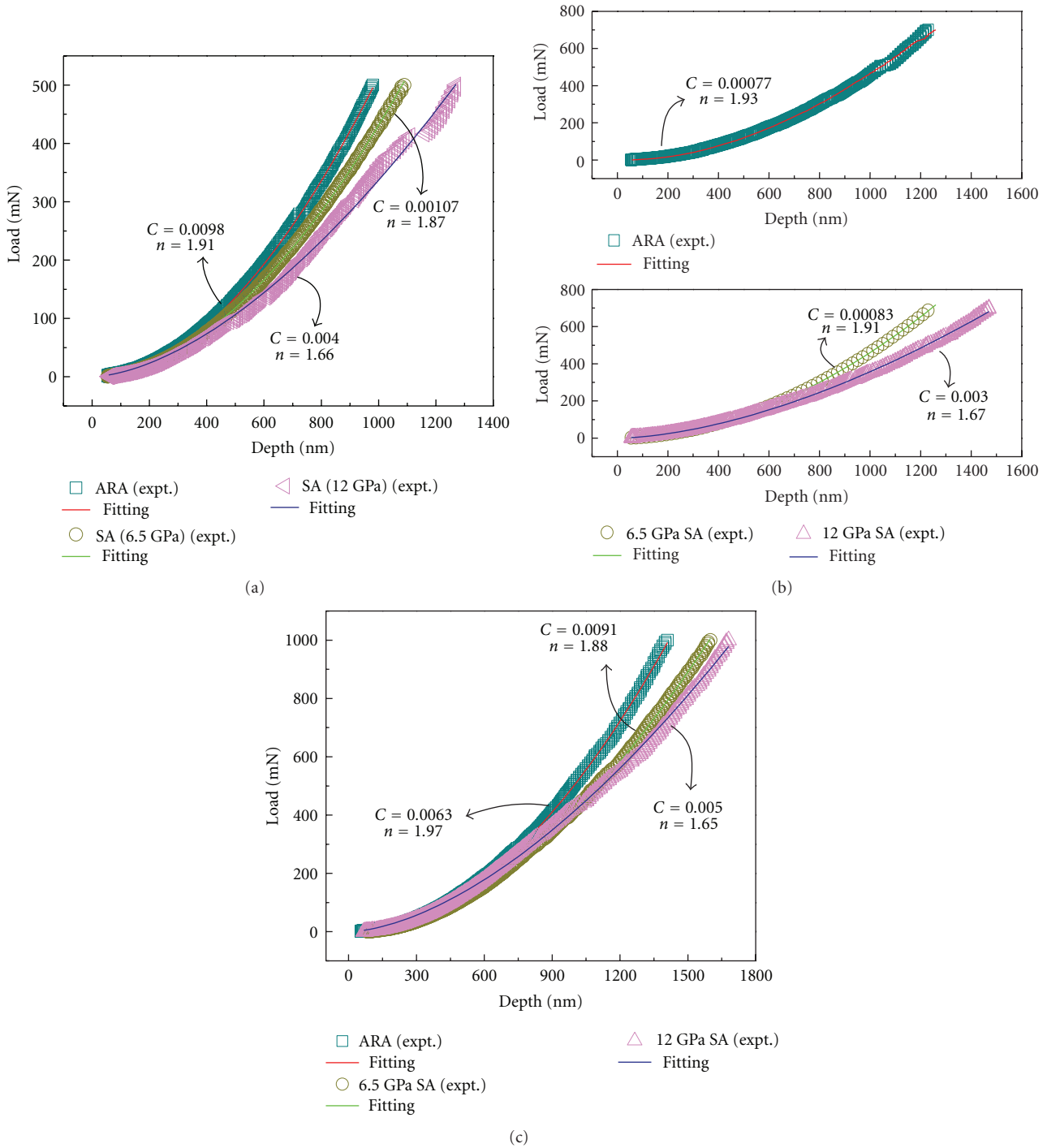


FIGURE 3: Fitting of the empirical equation $P = Ch^n$ to the load (P) versus depth (h) data of loading cycles during nanoindentation at typical, illustrative peak loads of (a) 500 mN, (b) 700 mN, and (c) 1000 mN for ARA, 6.5 GPa SA, and 12 GPa SA, samples. The solid lines depict the fit.

the theoretical It is interesting to note that the slip bands in SA sample were oriented parallel to the surface of the wall in the nanoindentation cavity (Figures 6(b) and 6(c)). Therefore, based on the theoretical modeling work [25] as discussed earlier and the present FE-SEM base evidences (Figure 6), a relatively stronger ISE was expected in the SA samples, as was also experimentally observed (Figure 2(b)).

The shear stress required for initiation of the nanoscale displacement jumps will have to be provided by the nanoindentation process itself. Because of the intense local stress distribution inside the nanoindentation cavity, the strain is expected to be very high, and its spatial gradient would be significantly large, especially near the base of the nanoindentation cavity. Given the knowledge of the

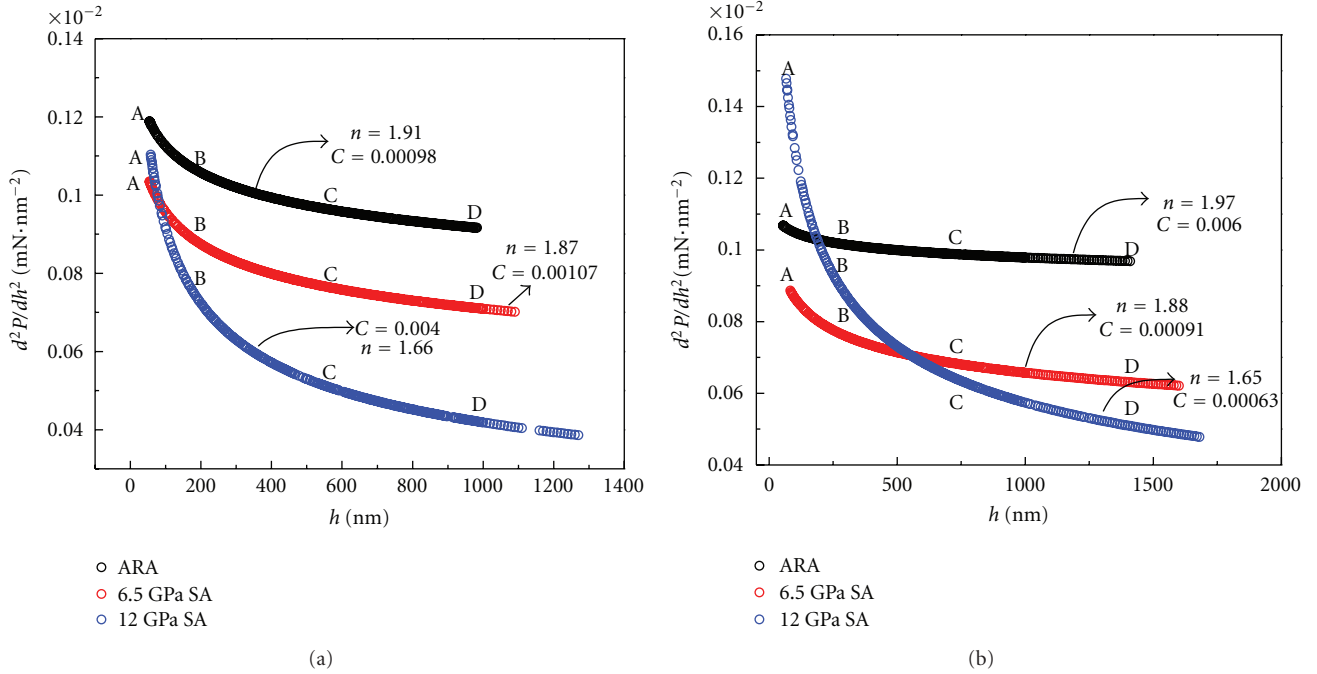


FIGURE 4: Variation of d^2P/dh^2 as a function of depth (h) for ARA, 6.5 GPa SA and 12 GPa SA samples at typical, illustrative nanoindentation peak loads of (a) 500 mN and (b) 1000 mN. The solid lines depict the fit.

TABLE 1: The relative percentages of changes in d^2P/dh^2 versus depth (h) plots of Figure 4 along AB, BC and CD at a typical illustrative nanoindentation peak loads of 500 mN and 1000 mN for ARA, 6.5 GPa SA and 12 GPa SA samples.

Loads (mN)	Sample	AB (%)	BC (%)	CD (%)
500	ARA	10.39	9.42	4.37
	6.5 GPa SA	15.34	13.06	6.80
	12 GPa SA	34.38	30.55	17.24
1000	ARA	4.32	2.58	2.32
	6.5 GPa SA	14.32	10.71	7.68
	12 GPa SA	39.89	27.62	20.44

geometric and elastic properties of the indenter and sample [45–47], the maximum shear stress, τ_{\max} , generated just below the nanoindenter tip can be calculated. The load at which the first burst is observed in the P - h plot was utilized for this purpose because it can be directly linked to the initiation of dislocation nucleation [45, 46]. Thus, the appropriate load values at which the first displacement bursts had occurred were obtained from the respective P - h plots of the ARA and the SA samples. A typical illustrative example is shown in Figure 7 for ARA, 6.5 GPa SA, and 12 GPa SA samples at a typical load of 100 mN. These load values are termed as the critical load values (P_c) and are plotted as a function of the nanoindentation loads, P in Figure 8(a). It is well appreciated that at ultralow loads causing shallow indentation displacements (e.g., at depths of ~ 50 – 90 nm, insets of Figures 7(a)–7(c)), the tip radius even for the nominally sharp Berkovich tip (e.g., 150 nm tip radius) will

exert a significant contribution to the deformation process. Considering the fact that both the critical load (P_c) and the corresponding critical depth (h_c) data were of very small magnitude (e.g., $P_c \leq 0.4$ – 1 mN, Figure 8(a), $h_c \sim 50$ – 90 nm, Figures 7(a)–7(c)) and following the method adopted by other researchers for nanoindentation of polycrystalline alumina and sapphire [48, 49], the tip was approximated as a spherical indenter for the sake of simplicity. Thus, following [46, 47] and taking the appropriate critical load (P_c) values from the experimental data (Figure 8(a)), the maximum shear stress (τ_{\max}) values active just underneath the tip of the nanoindenter were evaluated (Figure 8(b)) for the given nanoindentation load range of 10–1000 mN. The maximum shear stress (τ_{\max}) was ~ 20 – 30 GPa for the ARA sample but dropped to ~ 20 GPa for both of the SA samples, Figure 8(b). Nevertheless, these data were much higher than the theoretical shear strength (τ_{theor}) of the alumina ceramic, that is, ~ 3 GPa [1]. Therefore, it is evident that the applied load provided enough shear stress to cause shear-induced flow and/or deformation as well as localized microcracking and/or microfracture in the nanoindented alumina ceramics. Thus, there was a strong possibility that the first bursts, as observed in the experimental P - h data plots (Figures 5 and 7), indeed corresponded to the initiation of nanoscale plasticity events in the present alumina ceramics, for example, through the nucleation of shear bands, Figure 6 [38–47].

The frequent presence of multiple “*micro pop-in*” events in the P - h plots of both of the SA samples suggest a generic mechanism which was responsible for the experimental observation of a relatively stronger ISE in them. Such a mechanism will have its genesis linked to the relative frequency of the multiple “*micro pop-in*” events that occur

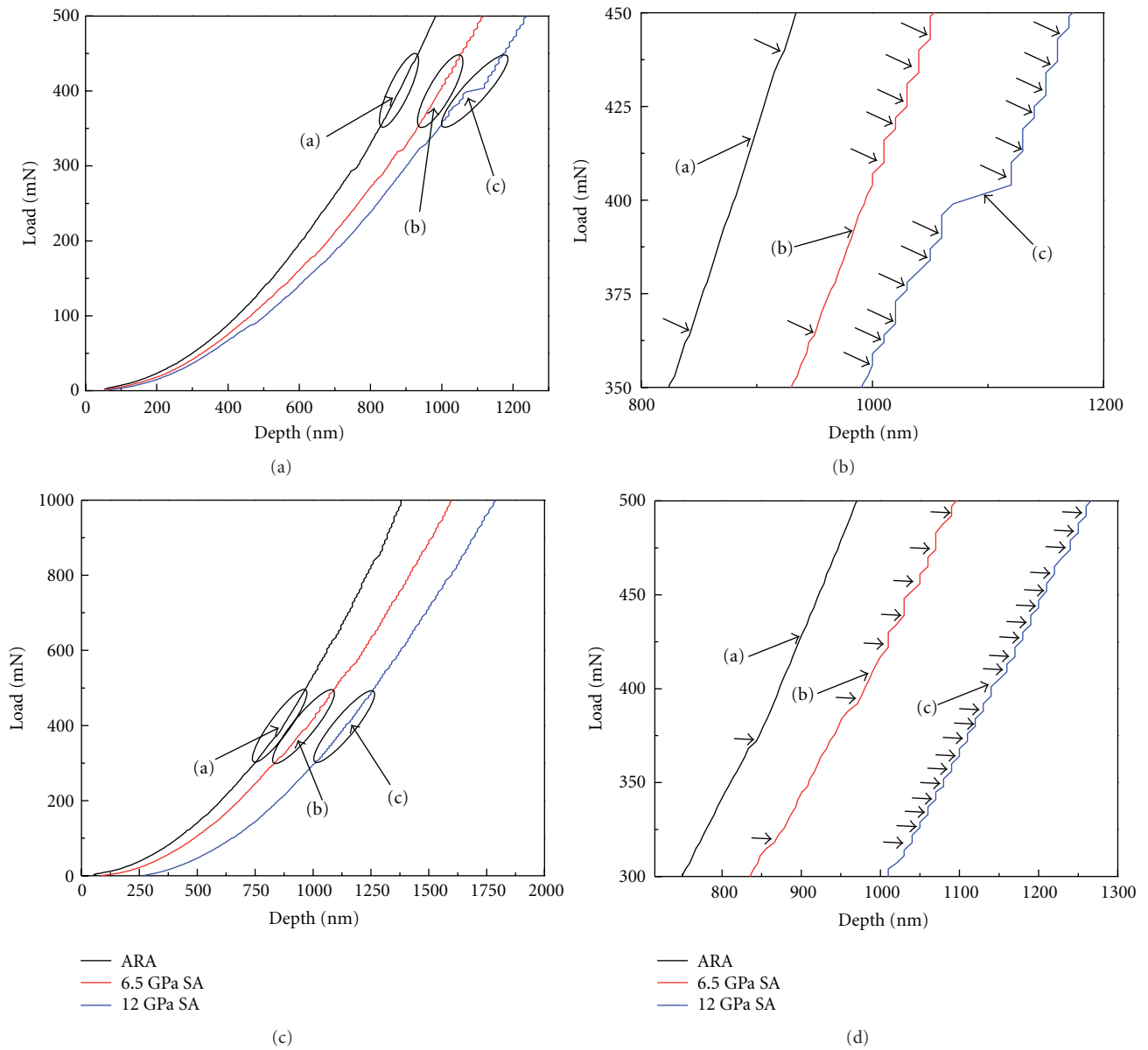


FIGURE 5: Typical load (P) versus depth (h) plots showing the details of serrations during loading cycles in experiments on ARA, 6.5 GPa SA, and 12 GPa SA samples at typical peak nanoindentation loads of 500 and 1000 mN: (a, c) normal view and (b, d) enlarged view.

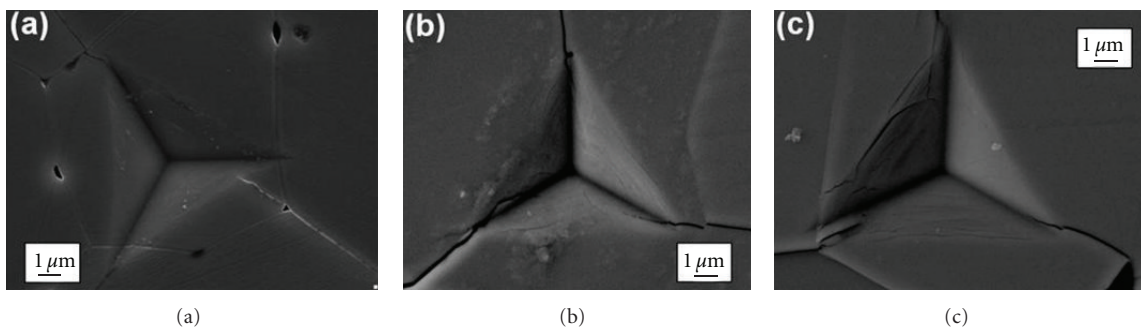


FIGURE 6: Typical FE-SEM of nanoindentation impressions in (a) ARA, (b) 6.5 GPa SA, and (c) 12 GPa SA samples [28, 30].

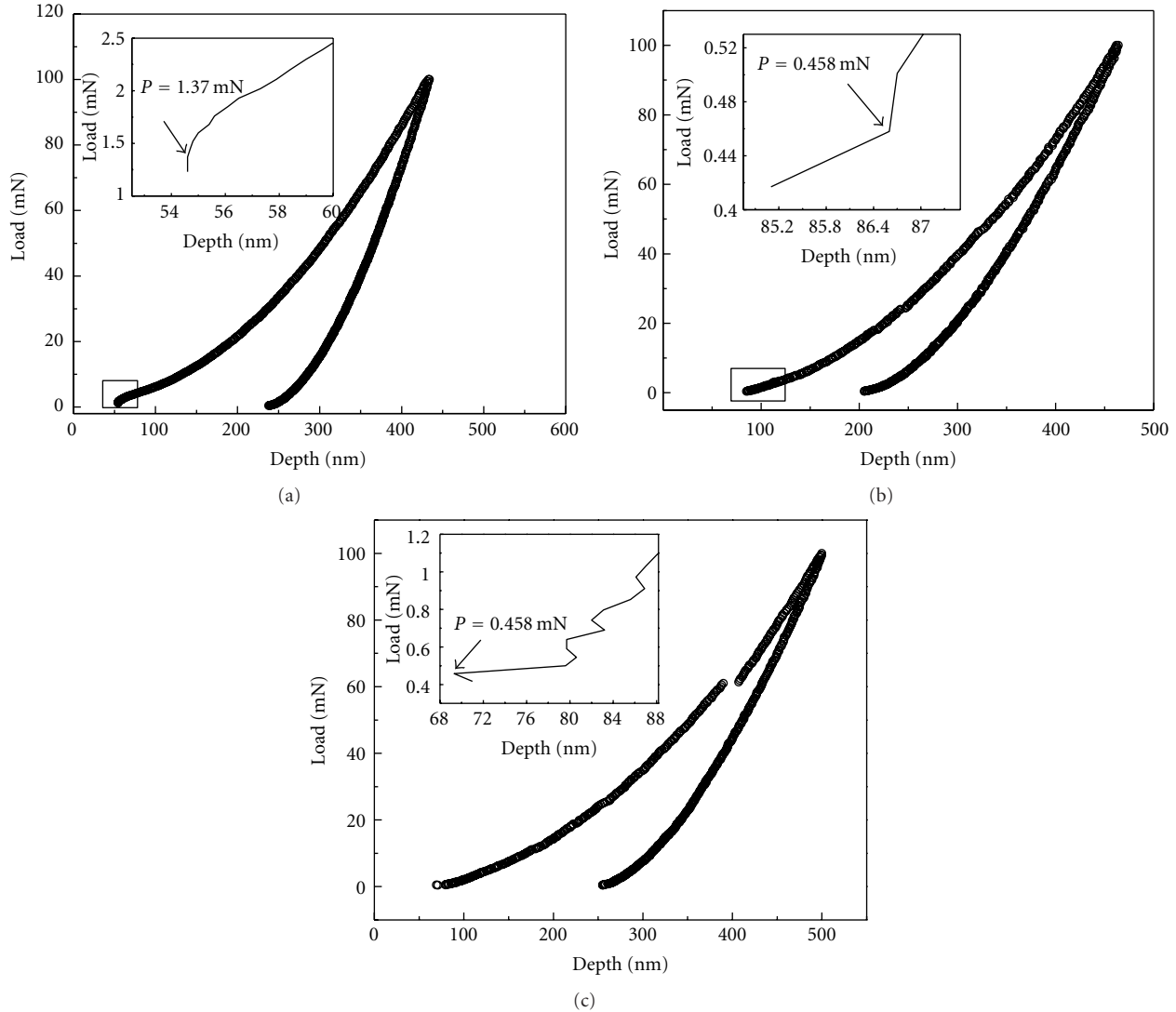


FIGURE 7: At an illustrative load of 100 mN, the typical signatures of serrations in loading cycles of load (P) versus depth (h) plots of (a) ARA, (b) 6.5 GPa SA, and (c) 12 GPa SA samples (insets in these pictures show typically illustrate how the first critical loads (P_c) and the critical depths (h_c) at which the displacement bursts had occurred.

at the microstructural and/or nanostructural length scale, as a function of the applied nanoindentation load. *In reality though*, a multitude of factors may control the frequency of such multiple “*micro pop-in*” events physically. The most important of such factors can be suggested as (a) how the microtensile stresses are spatially distributed in the vicinity of the nanoindentation cavity, (b) what is the relative orientation of a single grain and/or an assembly of multiple grains that encompass the microstructural damages and/or damage zones with respect to the nanoindentation loading direction, (c) the relative size of the nanoindentation cavity with respect to the size distribution of the pre-existent and shock-induced damages, (d) the relative orientation of the nanoindentation loading direction with respect to the spatial distribution of the pre-existent and shock induced damages, (e) the relative size of the “*characteristic length scale*” with respect to the grain thickness in the direction

of travel of the nanoindenter, (f) the presence or absence of residual strain due to shock loading, (g) the probability of microcrack generation during loading, and so forth. Therefore, the relative frequencies of the multiple “*micro pop-in*” events will actually control the relative rate of penetration by the nanoindenter in a given alumina ceramic microstructure. In turn, therefore; the relative extent of the indentation size effect will be controlled by this relative rate of penetration by the nanoindenter. On the other hand, FE-SEM photomicrographs showed confirmatory evidence of nanoscale slip band formation (denoted by white hollow arrowhead) in a suitably oriented single grain (Figure 9(a)), shear-induced intragrain microcrack formation (denoted by white solid arrowhead) in a single grain (Figure 9(b)) and extensive shear-induced complex intragranular microcleavage (denoted by “MC” with a single-line arrow) (Figure 9(c)) in SA samples obtained from 6.5 GPa shock experiments,

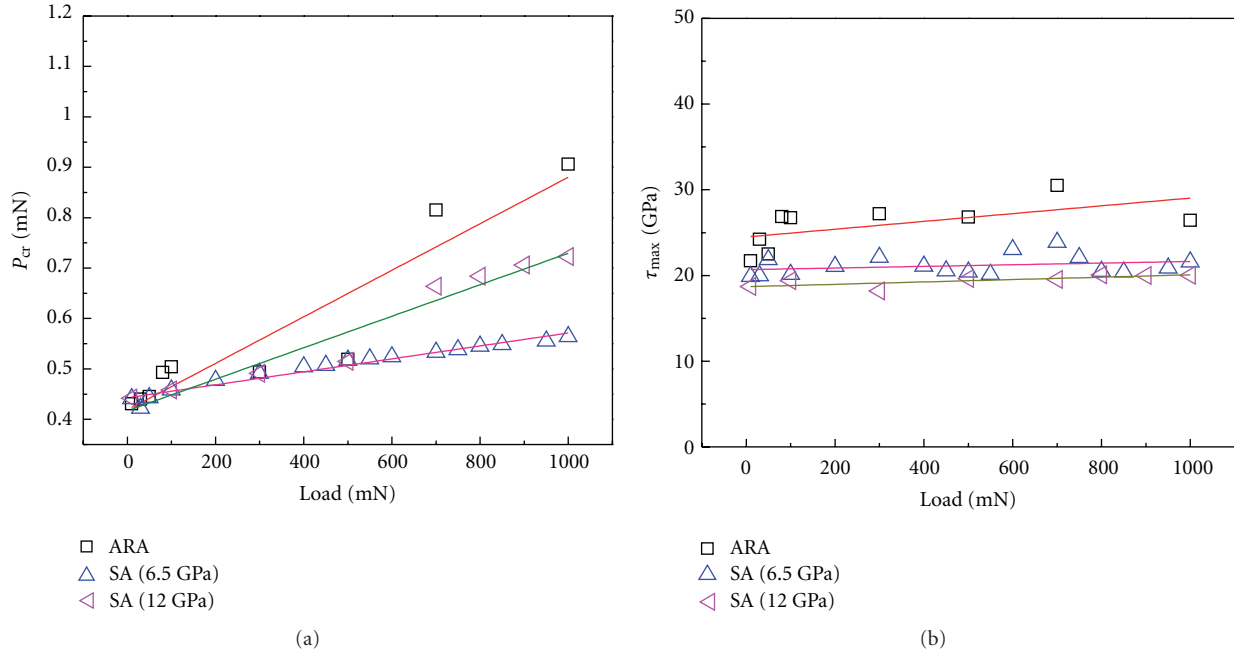


FIGURE 8: Variations of (a) critical load (P_c) and (b) maximum shear stress (τ_{max}) active just below the nanoindenter as a function of load (P) for ARA, 6.5 GPa SA, and 12 GPa SA samples.

as noted earlier also [28]. At a higher shock pressure of 12 GPa, the SA samples showed more FE-SEM-based evidences of extensive grain localized shear band formation (denoted by white hollow arrowhead) and grain boundary microcracking (denoted by white solid arrowhead) (Figures 9(d) and 9(e)) as well as very complex intragranular microcleavage (denoted by “MC” with a single line arrow) (Figure 9(f)), where individual cleavage planes are only 10–20 nm thick. All these evidences (Figure 9) point towards the extraordinary importance of nanoscale plasticity, shear-induced *localized* deformation and microfracture events in the SA samples during the present nanoindentation experiments. Additional support for nanoscale plasticity events, for example, nucleation of dislocations, and so forth, stem from the TEM photomicrograph-based evidences presented elsewhere [27–31] for the present SA samples. The TEM-based studies reported by us in [28] for alumina shock deformed at 6.5 GPa showed evidences of: (a) dislocations in a single alumina grain, (b) entanglement of dislocations, (c) dislocation network, and (d) dislocations at an impeded grain boundary. Similarly, the TEM-based investigations reported by us in [30] for alumina shock deformed at 12 GPa showed evidence of dislocation entanglements at triple-grain junction and grain edge as well as stacking fault inside a single grain. These evidences [28, 30] proved the extensive presence of microstructural damages in the SA samples. Such microstructural damages can lead to generation of highly localized microtensile strain in the microstructure thereby making it more compliant.

Finally, the whole scenario of the nanoindentation responses of the ARA and the SA samples can be explained by a qualitative model (Figures 10(a)–10(c)) proposed earlier

[28, 30] by us. The model basically involves three issues: (i) the spatial distribution of microstructural scale, processing induced defects, which has a statistical distribution of size and shape present in the ARA samples, (ii) the spatial, statistical distribution of additional shock induced microstructural defects evolves in the SA samples, and (iii) the probability of interaction between the “*microstructural defects*” and the “*zone of influence*” which depends on the load applied on the penetrating nanoindenter. Of these two, obviously the alumina shock deformed at 6.5 GPa has defect density (Figure 10(b)) higher than that of the ARA sample (Figure 10(a)), while the alumina shock deformed at 12 GPa has the highest defect density (Figure 10(c)).

At lower load of indentation, the probability of interaction between the “*microstructural defects*” and the penetrating nanoindenter is much lesser which is only slightly enhanced at a relatively higher load of indentation thereby providing a mild ISE in ARA samples (Figure 2(b)). Even at the same comparable lower loads of nanoindentation, the significant enhancement in “*microstructural defects*” density in the 6.5 GPa SA sample (Figures 9(a)–9(c) and 10(b)) increase by manifold the probability of interaction between them and the deformation volume underneath the penetrating nanoindenter in comparison to that of the ARA sample (Figure 10(a)). It is obvious that “*microstructural defects*” density was much higher in the SA samples shocked at 12 GPa (Figures 9(d)–9(f) and 10(c)) than at 6.5 GPa (Figures 9(a)–9(c) and 10(b)). So the nanoindenter-“*microstructural defects*” interaction was more severe in the SA samples shocked at 12 GPa (Figure 10(c)) than at 6.5 GPa (Figure 10(b)). The larger the interaction, the higher would be the rate of change of nanoindentation depth and hence

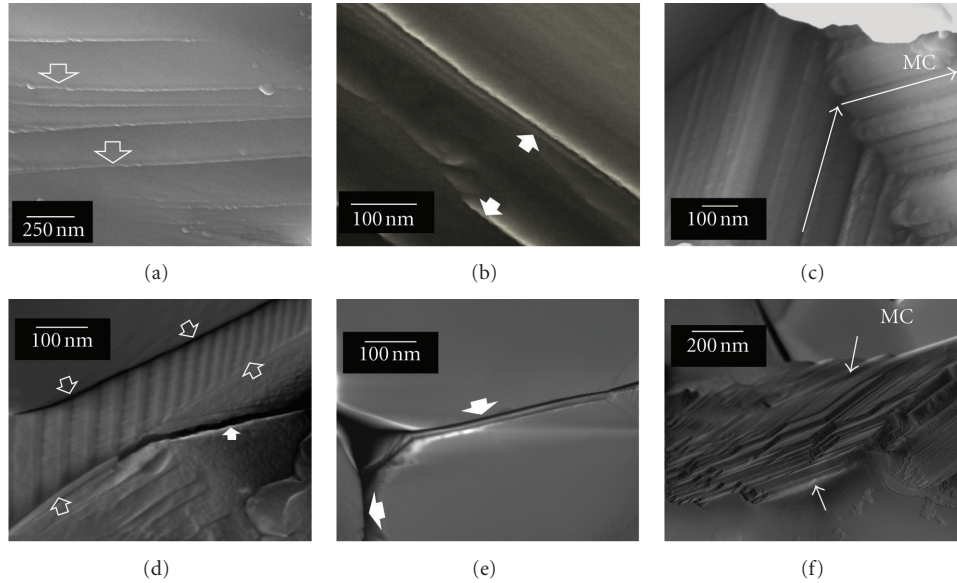


FIGURE 9: FE-SEM photomicrographs of SA samples obtained from 6.5 GPa (a, b, c) and 12 GPa (d, e, f) shock experiments: (a) nano scale slip band formation (denoted by white hollow arrowhead), (b) shear induced intra-grain microcrack formation (denoted by white solid arrowhead) in a single grain and (c) shear induced complex intragranular microcleavage (denoted by “MC” with a single-line arrow) (d) extensive grain localized shear band formation (denoted by white hollow arrowhead) and grain boundary microcracking (denoted by white solid arrowhead), (e) grain boundary microcracking (denoted by white solid arrowhead) and (f) very complex intragranular microcleavage (denoted by “MC” with a single line arrow).

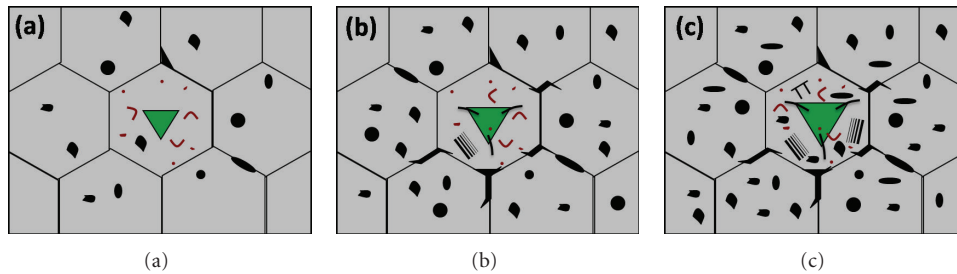


FIGURE 10: A qualitative model for the whole scenario of nanoindentation responses of (a) ARA (b) 6.5 GPa SA and (c) 12 GPa SA samples [28].

that of the projected area of contact. This is reflected in the more steeper decrease in nanohardness with depth in the case of SA samples shocked at 12 GPa (~33%) than at 6.5 GPa (~25%), Figure 2(b), before leveling off at much higher penetration depths (400–900 nm). This picture explains why the ISE was the strongest in the SA samples shocked at 12 GPa, stronger in the SA samples shocked at 6.5 GPa, and only mild in the ARA samples.

4. Conclusions

The major conclusions of the present work were the follows.

- (a) The nanohardness of the shocked alumina (SA) was about 25–30% lower than that of the as received alumina (ARA) sample. The Nix and Gao model could explain the strongest ISE in SA samples shocked at

12 GPa followed by that in the SA samples shocked at 6.5 GPa and mild ISE in the ARA sample.

- (b) For a given alumina ceramic microstructure, the relative extent of the ISE is controlled by the relative rate of penetration of the nanoindenter, governed by the relative frequency of the multiple “*micro pop-in*” events linked to the occurrences of shear bursts and/or subsequent generation of microcracks. The shear stress generated just underneath the nanoindenter had enough magnitude to cause shear-induced deformation as well as localized microcracking and/or microfracture in the nanoindented alumina ceramics.
- (c) A qualitative model based on the statistical distribution of characteristic microstructural defects in the ARA samples, the spatial distribution of additional

shock-induced microstructural defects present in the SA samples, and the probability of interaction between the “total microstructural defects” and the “nanoindentation volume” created by the penetrating nanoindenter depending on the applied load can successfully explain the overall nanoindentation behavior of the ARA and SA samples.

Acknowledgments

The authors acknowledge encouragements from Director, CGCRI and financial supports of BRNS (GAP 0219) and CSIR (Project nos.: NWP 0027 and NWP 0029; SRF ACK no.: 163055/2 K11/1).

References

- [1] Z. Rosenberg, D. Yaziv, Y. Yeshurun, and S. J. Bless, “Shear strength of shock-loaded alumina as determined with longitudinal and transverse manganin gauges,” *Journal of Applied Physics*, vol. 62, no. 3, pp. 1120–1122, 1987.
- [2] T. Mashimo, Y. Hanaoka, and K. Nagayama, “Elastoplastic properties under shock compression of Al₂O₃ single crystal and polycrystal,” *Journal of Applied Physics*, vol. 63, no. 2, pp. 327–336, 1988.
- [3] D. E. Grady, “Shock-wave compression of brittle solids,” *Mechanics of Materials*, vol. 29, no. 3–4, pp. 181–203, 1998.
- [4] M. W. Chen, J. W. McCauley, D. P. Dandekar, and N. K. Bourne, “Dynamic plasticity and failure of high-purity alumina under shock loading,” *Nature Materials*, vol. 5, no. 8, pp. 614–618, 2006.
- [5] G. R. Anstis, P. Chantikul, B. R. Lawn, and D. B. Marshall, “A critical evaluation of indentation techniques for measuring fracture toughness: I, direct crack measurements,” *Journal of the American Ceramic Society*, vol. 64, no. 9, pp. 533–538, 1981.
- [6] A. Krell and P. Blank, “Grain size dependence of hardness in dense submicrometer alumina,” *Journal of the American Ceramic Society*, vol. 78, no. 4, pp. 1118–1120, 1995.
- [7] A. Franco, S. G. Roberts, and P. D. Warren, “Fracture toughness, surface flaw sizes and flaw densities in Al₂O₃,” *Acta Materialia*, vol. 45, no. 3, pp. 1009–1015, 1997.
- [8] A. Krell and S. Schädlich, “Nanoindentation hardness of submicrometer alumina ceramics,” *Materials Science and Engineering A*, vol. 307, no. 1–2, pp. 172–181, 2001.
- [9] A. Krell, P. Blank, H. Ma, T. Hutzler, and M. Nebelung, “Processing of high-density submicrometer Al₂O₃ for new applications,” *Journal of the American Ceramic Society*, vol. 86, no. 4, pp. 546–553, 2003.
- [10] Q. Ma and D. R. Clarke, “Size dependent hardness of silver single crystals,” *Journal of Materials Research*, vol. 10, no. 4, pp. 853–863, 1995.
- [11] S. J. Bull, T. F. Page, and E. H. Yoffe, “An explanation of the indentation size effect in ceramics,” *Philosophical Magazine Letters*, vol. 59, no. 6, pp. 281–288, 1989.
- [12] N. K. Mukhopadhyay and P. Paufler, “Micro- and nanoindentation techniques for mechanical characterisation of materials,” *International Materials Reviews*, vol. 51, no. 4, pp. 209–245, 2006.
- [13] Z. Peng, J. Gong, and H. Miao, “On the description of indentation size effect in hardness testing for ceramics: analysis of the nanoindentation data,” *Journal of the European Ceramic Society*, vol. 24, no. 8, pp. 2193–2201, 2004.
- [14] E. O. Bernhardt, “On microhardness of solids at the limit of kick’s similarity law,” *Zeitschrift Fur Metallkunde*, vol. 33, no. 3, pp. 135–144, 1941 (German).
- [15] W. D. Nix and H. Gao, “Indentation size effects in crystalline materials: a law for strain gradient plasticity,” *Journal of the Mechanics and Physics of Solids*, vol. 46, no. 3, pp. 411–425, 1998.
- [16] M. F. Horstemeyer, M. I. Baskes, and S. J. Plimpton, “Length scale and time scale effects on the plastic flow of fcc metals,” *Acta Materialia*, vol. 49, no. 20, pp. 4363–4374, 2001.
- [17] A. Iost and R. Bigot, “Indentation size effect: reality or artefact?” *Journal of Materials Science*, vol. 31, no. 13, pp. 3573–3577, 1996.
- [18] H. Li, A. Ghosh, Y. H. Han, and R. C. Bradt, “The frictional component of the indentation size effect in low load microhardness testing,” *Journal of Materials Research*, vol. 8, no. 5, pp. 1028–1032, 1993.
- [19] M. V. Swain and M. Wittling, “Indentation cracking of brittle thin films on brittle substrates,” in *Fracture Mechanics of Ceramics*, R. C. Bradt, Ed., vol. 11, pp. 379–387, Plenum Press, New York, NY, USA, 1996.
- [20] J. Gong and Z. Guan, “Load dependence of low-load Knoop hardness in ceramics: a modified PSR model,” *Materials Letters*, vol. 47, no. 3, pp. 140–144, 2001.
- [21] Y. X. Gao and H. Fan, “A micro-mechanism based analysis for size-dependent indentation hardness,” *Journal of Materials Science*, vol. 37, no. 20, pp. 4493–4498, 2002.
- [22] A. Dey, A. K. Mukhopadhyay, S. Gangadharan, M. K. Sinha, and D. Basu, “Weibull modulus of nano-hardness and elastic modulus of hydroxyapatite coating,” *Journal of Materials Science*, vol. 44, no. 18, pp. 4911–4918, 2009.
- [23] C. Hays and E. G. Kendall, “An analysis of Knoop microhardness,” *Metallography*, vol. 6, no. 4, pp. 275–282, 1973.
- [24] H. Li and R. C. Bradt, “Knoop microhardness anisotropy of single-crystal LaB₆,” *Materials Science and Engineering A*, vol. 142, no. 1, pp. 51–61, 1991.
- [25] H. G. M. Kreuzer and R. Pippan, “Discrete dislocation simulation of nanoindentation: indentation size effect and the influence of slip band orientation,” *Acta Materialia*, vol. 55, no. 9, pp. 3229–3235, 2007.
- [26] T. M. Gross and M. Tomozawa, “Fictive temperature-independent density and minimum indentation size effect in calcium aluminosilicate glass,” *Journal of Applied Physics*, vol. 104, no. 6, Article ID 063529, 10 pages, 2008.
- [27] A. K. Mukhopadhyay, K. D. Joshi, A. Dey et al., “Shock deformation of coarse grain alumina above Hugoniot elastic limit,” *Journal of Materials Science*, vol. 45, no. 13, pp. 3635–3651, 2010.
- [28] R. Chakraborty, A. Dey, A. K. Mukhopadhyay et al., “Nanohardness of sintered and shock deformed alumina,” *Metallurgical and Materials Transactions A*, vol. 43, no. 2, pp. 459–470, 2012.
- [29] A. K. Mukhopadhyay, K. D. Joshi, A. Dey et al., “Electron microscopy of shock deformation in alumina,” *Ceramics International*, vol. 37, no. 7, pp. 2365–2376, 2011.
- [30] R. Chakraborty, A. Dey, A. K. Mukhopadhyay et al., “Indentation size effect of alumina ceramic shocked at 12 GPa,” *International Journal of Refractory Metals and Hard Materials*, vol. 33, pp. 22–32, 2012.
- [31] A. K. Mukhopadhyay, K. D. Joshi, A. Dey et al., “Nanoindentation of shock deformed alumina,” *Materials Science and Engineering A*, vol. 527, no. 24–25, pp. 6478–6483, 2010.

- [32] W. C. Oliver and G. M. Pharr, "An improved technique for determining hardness and elastic modulus using load and displacement sensing indentation experiments," *Journal of Materials Research*, vol. 7, no. 6, pp. 1564–1583, 1992.
- [33] D. Chakravarty, S. Bysakh, K. Muraleedharan, T. N. Rao, and R. Sundaresan, "Spark plasma sintering of magnesia-doped alumina with high hardness and fracture toughness," *Journal of the American Ceramic Society*, vol. 91, no. 1, pp. 203–208, 2008.
- [34] Y. Huang, F. Zhang, K. C. Hwang, W. D. Nix, G. M. Pharr, and G. Feng, "A model of size effects in nano-indentation," *Journal of the Mechanics and Physics of Solids*, vol. 54, no. 8, pp. 1668–1686, 2006.
- [35] T. Ebisu and S. Horibe, "Analysis of the indentation size effect in brittle materials from nanoindentation load-displacement curve," *Journal of the European Ceramic Society*, vol. 30, no. 12, pp. 2419–2426, 2010.
- [36] A. C. Fischer-Cripps, "Critical review of analysis and interpretation of nanoindentation test data," *Surface and Coatings Technology*, vol. 200, no. 14–15, pp. 4153–4165, 2006.
- [37] M. Sakai, "Energy principle of the indentation-induced inelastic surface deformation and hardness of brittle materials," *Acta Metallurgica et Materialia*, vol. 41, no. 6, pp. 1751–1758, 1993.
- [38] G. Subhash, S. Maiti, P. H. Geubelle, and D. Ghosh, "Recent advances in dynamic indentation fracture, impact damage and fragmentation of ceramics," *Journal of the American Ceramic Society*, vol. 91, no. 9, pp. 2777–2791, 2008.
- [39] D. J. Morris, S. B. Myers, and R. F. Cook, "Sharp probes of varying acuity: instrumented indentation and fracture behavior," *Journal of Materials Research*, vol. 19, no. 1, pp. 165–175, 2004.
- [40] J. S. Field, M. V. Swain, and R. D. Dukino, "Determination of fracture toughness from the extra penetration produced by indentation-induced pop-in," *Journal of Materials Research*, vol. 18, no. 6, pp. 1412–1419, 2003.
- [41] G. D. Quinn, P. Green, and K. Xu, "Cracking and the indentation size effect for knoop hardness of glasses," *Journal of the American Ceramic Society*, vol. 86, no. 3, pp. 441–448, 2003.
- [42] R. Nowak, T. Sekino, and K. Niihara, "Surface deformation of sapphire crystal," *Philosophical Magazine A*, vol. 74, no. 1, pp. 171–194, 1996.
- [43] J. E. Bradby, S. O. Kucheyev, J. S. Williams et al., "Indentation-induced damage in GaN epilayers," *Applied Physics Letters*, vol. 80, no. 3, pp. 383–385, 2002.
- [44] S. O. Kucheyev, J. E. Bradby, J. S. Williams, C. Jagadish, and M. V. Swain, "Mechanical deformation of single-crystal ZnO," *Applied Physics Letters*, vol. 80, no. 6, pp. 956–958, 2002.
- [45] H. Bei, Z. P. Lu, and E. P. George, "Theoretical strength and the onset of plasticity in bulk metallic glasses investigated by nanoindentation with a spherical indenter," *Physical Review Letters*, vol. 93, no. 12, Article ID 125504, 4 pages, 2004.
- [46] C. E. Packard and C. A. Schuh, "Initiation of shear bands near a stress concentration in metallic glass," *Acta Materialia*, vol. 55, no. 16, pp. 5348–5358, 2007.
- [47] H. Shang, T. Rouxel, M. Buckley, and C. Bernard, "Viscoelastic behavior of a soda-lime-silica glass in the 293–833 K range by micro-indentation," *Journal of Materials Research*, vol. 21, no. 3, pp. 632–638, 2006.
- [48] W. G. Mao, Y. G. Shen, and C. Lu, "Deformation behavior and mechanical properties of polycrystalline and single crystal alumina during nanoindentation," *Scripta Materialia*, vol. 65, no. 2, pp. 127–130, 2011.
- [49] W. G. Mao, Y. G. Shen, and C. Lu, "Nanoscale elastic-plastic deformation and stress distributions of the C plane of sapphire single crystal during nanoindentation," *Journal of the European Ceramic Society*, vol. 31, no. 10, pp. 1865–1871, 2011.



Hindawi

Submit your manuscripts at
<http://www.hindawi.com>

